



## Development of a bimodal structure in ocean wave spectra

A. Toffoli,<sup>1,2</sup> M. Onorato,<sup>3</sup> E. M. Bitner-Gregersen,<sup>1</sup> and J. Monbaliu<sup>4</sup>

Received 6 May 2009; revised 25 August 2009; accepted 1 October 2009; published 3 March 2010.

[1] Traditionally, the directional distribution of ocean waves has been regarded as unimodal, with energy concentrated mainly on the wind direction. However, numerical experiments and field measurements have already demonstrated that the energy of short waves tends to be accumulated along two off-wind directions, generating a bimodal directional distribution. Here, numerical simulations of the potential Euler equations are used to investigate the temporal evolution of initially unimodal directional wave spectra. Because this approach does not include external forcing such as wind and breaking dissipation, spectral changes are only driven by nonlinear interactions. The simulations show that the wave energy spreads outward from the spectral peak, following two characteristic directions. As a result, the directional distribution develops a bimodal form as the wavefield evolves. Although bimodal properties are more pronounced in the high wave number part of the spectrum, in agreement with previous field measurements, the simulations also show that directional bimodality characterizes the spectral peak.

**Citation:** Toffoli, A., M. Onorato, E. M. Bitner-Gregersen, and J. Monbaliu (2010), Development of a bimodal structure in ocean wave spectra, *J. Geophys. Res.*, 115, C03006, doi:10.1029/2009JC005495.

### 1. Introduction

[2] The most common expressions for the directional distribution of the wave energy spectrum are based on the parameterization of field data [see, e.g., Mitsuyasu *et al.*, 1975; Hasselmann *et al.*, 1980; Donelan *et al.*, 1985]. In the resulting directional spreading functions, the wave energy is concentrated mainly on the wind direction (mean wave direction) and decreases monotonically in off-wind directions, i.e., the directional distribution is unimodal. Nevertheless, there is evidence for the concentration of wave energy in off-wind directions in the high-frequency tail of the spectrum [see, e.g., Phillips, 1958; Côté *et al.*, 1960; Holthuijsen, 1983; Jackson *et al.*, 1985; Wyatt, 1995; Young *et al.*, 1995; Ewans, 1998; Hwang *et al.*, 2000; Wang and Hwang, 2001; Long and Resio, 2007] (among others).

[3] Without considering external forcing, Longuet-Higgins [1976] investigated the nonlinear energy transfer at the spectral peak using the Davey and Stewartson [1974] equation, which provides a description of the evolution of three-dimensional wave packets under the narrowbanded assumption (both in frequency and direction). Beside a flux of energy toward high and low frequencies (or wave numbers) at the expense of large energy loss near the peak [cf. Hasselmann, 1962], he found that there is the tendency

for the wave energy to spread outward from the spectral peak along two characteristic directions, forming angles of  $\pm\arctan(1/\sqrt{2})$  rad (i.e.,  $\pm 35.5^\circ$ ) with the mean wave direction. In agreements with such results, Dysthe *et al.* [2003] observed that an initial Gaussian-shaped spectrum expands toward two characteristics directions, using three-dimensional numerical simulations of the nonlinear Schrödinger (NLS) equation. It is however important to stress that these findings were obtained under the hypothesis that the wave spectrum is narrow banded. Therefore, the results may be uncertain in oceanic wavefields, where the spectral energy is usually concentrated on a wide range of frequencies and directions (broadbanded sea states).

[4] More generally, the evolution of the wave spectrum, including the effect of wind, breaking dissipation, and nonlinear interactions, can be described by the energy transfer equation [Hasselmann, 1962]. Performing a series of numerical experiments on the basis of this equation, Komen *et al.* [1984], Young and Van Vledder [1993], and Banner and Young [1994] suggested that the directional spreading is mainly controlled by the action of the nonlinear energy transfer. In particular, apart from a general angular broadening at high frequencies, Banner and Young [1994] also observed that the energy of short waves accumulates over two sidelobes symmetrically located about the mean wave direction. As a result, in contrast to the unimodal spreading functions [Mitsuyasu *et al.*, 1975; Hasselmann *et al.*, 1980; Donelan *et al.*, 1985], the directional distribution develops a bimodal structure at frequencies greater than the spectral peak frequency.

[5] A first confirmation of the existence of a bimodal shape in ocean wave spectra was given by Young *et al.* [1995], who found good agreement between numerical simulations of the energy transfer equation and records of

<sup>1</sup>Det Norske Veritas A.S., Høvik, Norway.

<sup>2</sup>Now at Faculty of Engineering and Industrial Sciences, Swinburne University of Technology, Hawthorn, Victoria, Australia.

<sup>3</sup>Dipartimento Fisica Generale, Università di Torino, Turin, Italy.

<sup>4</sup>Department of Civil Engineering, Katholieke Universiteit Leuven, Heverlee, Belgium.

the directional distribution in fetch-limited conditions. A few years later, *Ewans* [1998] used directional buoy data to investigate the bimodal features of the directional distribution for stationary wind and wavefields under fetch-limited conditions. Despite the limitation of the processing technique (he used the maximum entropy method, which tends to produce narrower spectra with false bimodal directional distribution [*Lygre and Krogstad*, 1986]), his observations of the angular position of the sidelobes were in agreement with the full solution of the nonlinear wave-wave interaction source term [cf. *Young et al.*, 1995]. Moreover, the bimodal structure observed by *Ewans* [1998] was qualitatively consistent with observations of directional wave spectra which were obtained from high-resolution spatial measurements of the three-dimensional topography of ocean waves, during quasi steady wind conditions [*Hwang et al.*, 2000].

[6] Despite the fact that the existence of sidelobes, and hence the bimodal structure of the short-wave part of the spectrum, is a robust, distinctive, and persistent feature of ocean waves, a direct comparison of the measurements by *Ewans* [1998], *Hwang et al.* [2000], and records of directional wave spectra collected at Lake Michigan [see *Wang and Hwang*, 2001] showed that there is still some disagreement on the shape of the bimodal structure, i.e., location and amplitude of the sidelobes. In this respect, although the location of the spectral lobes seems to be consistent with the  $\pm 35.5^\circ$  direction calculated by *Longuet-Higgins* [1976] [see also *Janssen*, 2004], a direct comparison between this theoretical finding and the location of the sidelobes has not been discussed yet. It is also important to mention that not only the nonlinear transfer but also the inviscid critical-layer mechanism for the transfer of energy from the wind to the wave may give rise to bimodal directional distributions, especially for sufficiently high wind speed [*Morland*, 1996]. This conjecture is consistent with numerical simulations of the energy balance equation by *Alves and Banner* [2003], who observed the importance of the wind input term in shaping the bimodal angular distribution of the wind sea spectrum.

[7] In the present paper, we study in details the shape of the bimodal structure as a consequence of the nonlinear energy transfer only. In order to accomplish this task, we traced the temporal evolution of random, deep water, directional wavefields by integrating numerically the potential Euler equations for surface gravity waves. A higher-order spectral method (HOSM) [*Dommermuth and Yue*, 1987; *West et al.*, 1987] was used to this end. We mention that, apart from the order of the expansion implemented in the model, the equations do not have any bandwidth constraints unlike Schrödinger-type equations. Note also that this approach does not consider any forcing such as wind input or breaking dissipation. Thus, nonlinear interaction is the only mechanism involved. From one side, we want to verify whether the energy is redistributed along a  $\pm 35.5^\circ$  direction as suspected by *Longuet-Higgins* [1976] in both ideal narrowbanded and more realistic broadbanded spectral conditions and confirm the role of such redistribution in shaping the bimodal structure. From the other side we want to test the ability of the nonlinear energy transfer to approximate in situ measurements of the bimodal structure of the short-wave portion of the wave spectrum [*Ewans*, 1998; *Hwang et al.*, 2000], where effects of wind input,

nonlinear interaction, and wave dissipation are contemporarily present.

[8] The paper is organized as follows. A description of the numerical scheme and the experiments performed for this study is presented in section 2. The characteristics of the nonlinear energy transfer are discussed in section 3. The effect of the energy redistribution on the development of the wave energy spectrum and the properties of the sidelobes are addressed in sections 4 and 5. Some concluding remarks are presented in the section 6.

## 2. Numerical Experiment

### 2.1. Higher-Order Spectral Method

[9] The temporal evolution of directional wavefields is here modeled by the numerical integration of the potential Euler equations. Assuming the hypothesis of an irrotational, inviscid, and incompressible fluid flow, there exists a velocity potential  $\phi(x, y, z, t)$  which satisfies the Laplace equation everywhere in the fluid. We restrict ourselves to the case of domains with a constant water depth ( $h = \infty$  in this study). At the bottom ( $z = -h$ ) the boundary condition is such that the vertical velocity is zero ( $\phi_z|_{-h} = 0$ ). At the free surface ( $z = \eta(x, y, t)$ ), the kinematic and dynamic boundary conditions are satisfied for the free surface elevation and the velocity potential at the free surface  $\psi(x, y, t) = \phi(x, y, \eta(x, y, t), t)$ . Using the free surface variables, these boundary conditions are as follows [*Zakharov*, 1968]:

$$\psi_t + g\eta + \frac{1}{2}(\psi_x^2 + \psi_y^2) - \frac{1}{2}W^2(1 + \eta_x^2 + \eta_y^2) = 0, \quad (1)$$

$$\eta_t + \psi_x \eta_x + \psi_y \eta_y - W(1 + \eta_x^2 + \eta_y^2) = 0, \quad (2)$$

where the subscripts denote partial derivatives, and  $W(x, y, t) = \phi_z|_{\eta}$  represents the vertical velocity evaluated at the free surface.

[10] The time evolution of the surface elevation can be evaluated from equations (1) and (2). The numerical integration is performed by using the higher-order spectral method, which was independently proposed by *Dommermuth and Yue* [1987] and *West et al.* [1987]. A comparison of these two approaches [*Clamond et al.*, 2006] has shown that the formulation proposed by *Dommermuth and Yue* [1987] is less consistent than the one proposed by *West et al.* [1987]. The latter, therefore, has been applied for the present study.

[11] HOSM uses a series expansion in the wave slope of the vertical velocity  $W(x, y, t)$  about the free surface. Herein we considered a third-order expansion so that the four-wave interaction is included [see *Tanaka*, 2001a, 2007]. The expansion is then used to evaluate the velocity potential  $\psi(x, y, t)$  and the surface elevation  $\eta(x, y, t)$  from equations (1) and (2) at each instant of time. All aliasing errors generated in the nonlinear terms are removed by choosing the total number of mesh points in the  $x$  and  $y$  directions,  $N_x$  and  $N_y$ , respectively, such that the following conditions are satisfied (see *West et al.* [1987] and *Tanaka* [2001a] for details):  $Nk_x = N_x/(M+1)$  and  $Nk_y = N_y/(M+1)$ , where  $Nk_x$  and  $Nk_y$  are the numbers of mesh points free from aliasing errors in the spectral (wave number) space, and  $M$  is the order of the expansion ( $M = 3$  in this study). The time integration is then performed by means of a fourth-order

Runge–Kutta method. A small time step,  $\Delta t = T_p/200$  (where  $T_p$  is the peak period), is used to minimize the energy leakage. The accuracy of the computation is checked by monitoring the variation of the total energy [see, e.g., *Tanaka*, 2001b]. Despite the fact that the energy content shows a decreasing trend throughout the simulation, its variation is negligible as the relative error in total energy does not exceed 0.4% [cf. *Toffoli et al.*, 2008].

[12] Note that HOSM has already been used to investigate the evolution of directional wavefields by several authors [e.g., *Tanaka*, 2001a, 2007; *Onorato et al.*, 2002]. However, other numerical approaches can also be found in the literature; see, for example, *Tsai and Yue* [1996] and *Clamond et al.* [2006] for a review.

## 2.2. Initial Conditions

[13] For the definition of the initial conditions, a directional wave spectrum  $E(\omega, \theta) = S(\omega) D(\omega, \theta)$  is used, where  $S(\omega)$  represents the frequency spectrum and  $D(\omega, \theta)$  is the directional function. The energy distribution in the frequency domain was described by using the JONSWAP formulation [see, e.g., *Komen et al.*, 1994]:

$$S(\omega) = \frac{\alpha g^2}{\omega^5} \exp \left[ -\frac{5}{4} \left( \frac{\omega}{\omega_p} \right)^{-4} \right] \gamma \exp \left[ \frac{(\omega - \omega_p)^2}{(2\sigma^2 \omega_p^2)} \right], \quad (3)$$

where  $\omega$  is the angular frequency and  $\omega_p$  is the peak frequency; the parameter  $\sigma$  is equal to 0.07 if  $\omega \leq \omega_p$  and 0.09 if  $\omega > \omega_p$ . In the present study, for convenience, we selected the Phillips parameter  $\alpha = 0.016$ , peak enhancement factor  $\gamma = 6.0$ , and peak period  $T_p = 1$  s (any other wave period representing wind sea could be applied), which corresponds to a dominant wavelength  $\lambda_p = 1.56$  m. Such a configuration defines a wavefield with a significant wave height of 0.08 m and a wave steepness  $\varepsilon = k_p a = 0.08$ , where  $k_p$  is the wave number related to the dominant wavelength and  $a$  is a wave amplitude estimated as the square root of the spectral variance. A short peak period was chosen for convenience; any other combination of peak period (or wavelength) and significant wave height with similar steepness would lead to similar results. It is also important to mention that the selected spectra are characterized by a higher peakedness than that commonly observed in the ocean. We selected this condition because a large value of the peak enhancement factor emphasizes nonlinear effects (see, for example, *Onorato et al.* [2006] for details). For completeness, however, a few tests with lower peakedness, i.e.,  $\gamma = 1.0$  and 3.0, were also performed; note that reducing  $\gamma$  also slightly reduces the wave steepness.

[14] A  $\cos^{2s}(\vartheta/2)$  function was then applied to model the energy in the directional domain. The spreading coefficient  $s$  was assumed to be a function of the angular frequency; the following expression was used [*Mitsuyasu et al.*, 1975]:

$$s(\omega) = \left( \frac{\omega}{\omega_p} \right)^5 s_p \quad \text{for } \omega \leq \omega_p \quad (4)$$

$$s(\omega) = \left( \frac{\omega}{\omega_p} \right)^{-2.5} s_p \quad \text{for } \omega > \omega_p. \quad (5)$$

[15] Tests were run for different directional wavefields, ranging from fairly long to short crested conditions. In this respect, the spreading coefficient  $s$  was chosen such that at the peak frequency  $s_p = s(\omega_p) = 180, 48,$  and 24 (from long to short crested waves, respectively). Note, however, that the selected directional distributions are still rather narrow; in oceanic waters, for example,  $s_p = 24$  corresponds to swells [*Goda*, 2000]. For less-peaked spectra ( $\gamma = 1.0$  and 3.0), we only considered the case with  $s_p = 48$ .

[16] From the directional frequency spectrum,  $E(\omega, \theta)$ , an initial two-dimensional surface  $\eta(x, y, t = 0)$  was computed using first the linear dispersion relation to move from  $(\omega, \theta)$  to wave number coordinates  $(k_x, k_y)$ , and then the inverse Fourier transform with the random phase and amplitude approximation. In this respect, the random phases were uniformly distributed over the interval  $[0, 2\pi]$ , while the random amplitudes were Rayleigh distributed. The velocity potential was obtained from the input surface using linear theory. The wavefield was contained in a square domain of 14 m with spatial meshes of  $256 \times 256$  nodes; waves at the peak of the spectrum were assumed to propagate along the  $x$  direction. We mention that for this spatial configuration the dealiasing procedure removes wave numbers higher than six times the peak wave number.

[17] The total duration of the simulation was set equal to  $450 T_p$ ; the output sea surface,  $\eta(x, y, t)$ , was stored every  $50 T_p$ . In order to achieve statistically significant results, an ensemble of 120 repetitions using different random amplitudes and random phases were performed for each test. For further analysis, two-dimensional wave number spectra were calculated from the output surfaces as the ensemble average of the squared modulus of the Fourier coefficients; no smoothing was applied.

## 3. Nonlinear Energy Transfer

[18] The gradual transfer of energy between waves of different wavelengths (or frequencies) and directions is mainly due to resonances among particular groups of wave components [*Phillips*, 1960; *Hasselmann*, 1962]. For a random wavefield, the net rate of energy transfer to any one wave number resulting from its interactions with all others can be calculated in terms of the spectral density of wave action per unit mass [*Hasselmann*, 1962]:

$$\frac{\partial n_1}{\partial t} = \int \int \int G(\mathbf{k}_1, \mathbf{k}_2, \mathbf{k}_3, \mathbf{k}_4) [(n_1 + n_2)n_3 n_4 - (n_3 + n_4)n_1 n_2] \times \delta(\omega_1 + \omega_2 - \omega_3 - \omega_4) \delta(\mathbf{k}_1 + \mathbf{k}_2 - \mathbf{k}_3 - \mathbf{k}_4) d\mathbf{k}_2 d\mathbf{k}_3 d\mathbf{k}_4, \quad (6)$$

where  $n_i$  is the action density at wave number  $k_i$ ,  $\omega_i = \sqrt{g|k_i|}$  is the angular frequency, and  $G(\mathbf{k}_1, \mathbf{k}_2, \mathbf{k}_3, \mathbf{k}_4)$  is a coupling coefficient; the  $\delta$  functions express conditions for resonance between the waves  $i = 1, 2, 3, 4$ .

[19] The form of the coupling coefficient as given by *Hasselmann* is rather complicated. However, when all the wave numbers involved are nearly identical and equal to  $k_0$ , the coupling coefficient assumes a much simpler form [*Longuet-Higgins*, 1976]:

$$G = 4\pi k_0^6. \quad (7)$$

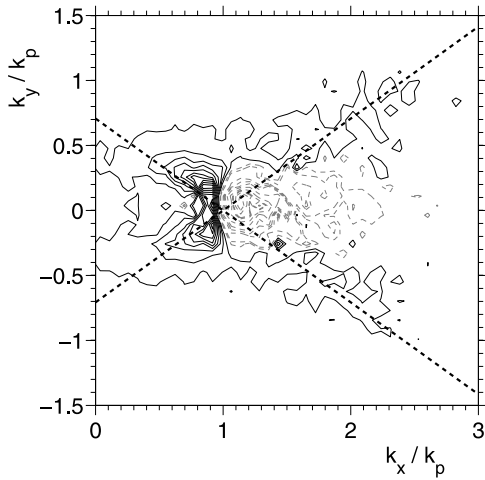


**Figure 1.** Simulated energy transfer for a wavefield with initial directional spreading  $s_p = 180$  and peak enhancement factor  $\gamma = 6.0$ : Positive transfer (solid line); negative transfer (dashed line);  $\pm 35.5^\circ$  directions [Longuet-Higgins, 1976] (thick dashed line).

[20] Under these circumstances, most of the energy transfer occurs among groups of almost identical wave numbers. Therefore, it can be expected to be most significant in the neighborhood of the spectral peak at wave number  $k_0$ . In this vicinity, equation (6) reduces to the following form:

$$\frac{\partial n_1}{\partial t} = 4\pi k_0^6 \int \int \int [(n_1 + n_2)n_3n_4 - (n_3 + n_4)n_1n_2] \times \delta(\omega_1 + \omega_2 - \omega_3 - \omega_4)\delta(\mathbf{k}_1 + \mathbf{k}_2 - \mathbf{k}_3 - \mathbf{k}_4)d\mathbf{k}_2d\mathbf{k}_3d\mathbf{k}_4. \quad (8)$$

[21] An interesting feature of equation (8) is that the energy tends to be transferred among wave numbers according to two characteristic directions at an angle of  $\pm 35.5^\circ$  with the mean wave direction. Note that this corresponds to the tangents to the figure-of-eight curve derived by Phillips [1960] just at the center point  $k_0$ . It is important to remark, however, that equation (8) is an approximation of the Hasselmann equation (6) for narrowbanded conditions. A detailed comparison between these two equations [Masuda, 1980] indicates that ordinary spectra may generally be too broad for Longuet-Higgins' model to be applicable.

[22] An estimation of the energy transfer can be obtained from the simulation of the temporal evolution of the surface elevation as follows [see Tanaka, 2001a]:

$$T(k_x, k_y) = \frac{E_{t_2}(k_x, k_y) - E_{t_1}(k_x, k_y)}{t_2 - t_1}, \quad (9)$$

where  $E_{t_1}(k_x, k_y)$  and  $E_{t_2}(k_x, k_y)$  are the wave number spectra of the surface elevation at times  $t_1$  and  $t_2$ , respectively. It is important to mention that our simulations describe the evolution of an imposed input surface. Thus, if a linear surface is used as initial condition, the first time steps are used to generate bound waves; this process approximately takes 10 peak periods [see Tanaka, 2001a, 2007]. Therefore, in order to consider energy transfer as a result of nonlinear wave-wave interactions, we estimated  $T(k_x, k_y)$  in the time

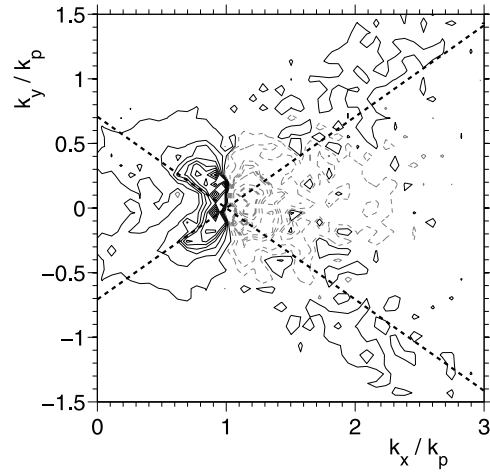


**Figure 2.** Simulated energy transfer for a wavefield with initial directional spreading  $s_p = 48$  and peak enhancement factor  $\gamma = 6.0$ : Positive transfer (solid line); negative transfer (dashed line);  $\pm 35.5^\circ$  directions [Longuet-Higgins, 1976] (thick dashed line).

interval between  $t_1 = 50 T_p$  and  $t_2 = 60 T_p$  (see, for a more detailed description on the estimation of the nonlinear energy transfer, Tanaka [2001a]). Figures 1–3 show the resulting energy transfer for the selected directional wavefields (initial  $\gamma = 6.0$ ); the two characteristic directions for the energy transfer as calculated by Longuet-Higgins [1976] are presented for comparison.

[23] The simulations show that a fraction of energy above the spectral peak is redistributed toward lower and higher wave numbers [cf. Hasselmann, 1962]. In qualitative agreement with Longuet-Higgins [1976], the energy transfer occurs along two characteristic directions oblique to the mean wave direction (note that the latter is represented by the  $k_x$  axis in wave number space, as waves were assumed to propagate in the  $x$  direction). For a long crested wavefield

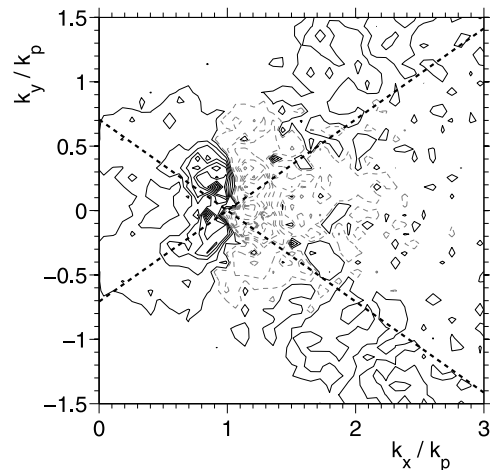


**Figure 3.** Simulated energy transfer for a wavefield with initial directional spreading  $s_p = 24$  and peak enhancement factor  $\gamma = 6.0$ : Positive transfer (solid line); negative transfer (dashed line);  $\pm 35.5^\circ$  directions [Longuet-Higgins, 1976] (thick dashed line).

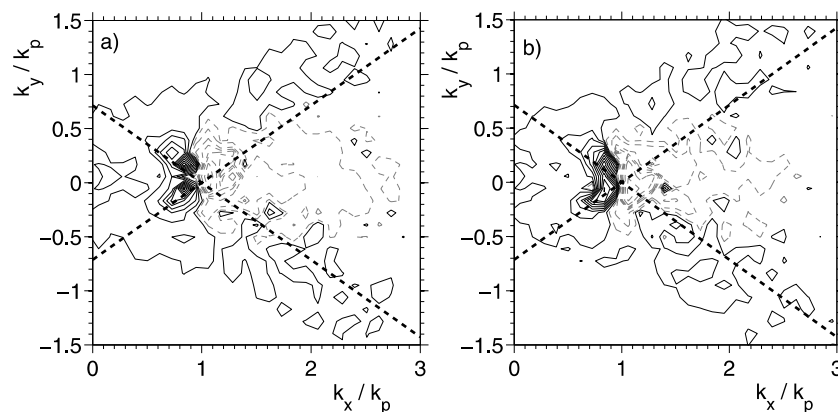


**Figure 4.** Simulated energy transfer for a wavefield with initial directional spreading  $s_p = 48$  and peak enhancement factor (a)  $\gamma = 1.0$  and (b)  $\gamma = 3.0$ : Positive transfer (solid line); negative transfer (dashed line);  $\pm 35.5^\circ$  directions [Longuet-Higgins, 1976] (thick dashed line).

( $s_p = 180$ ), these directions are consistent with the suggested  $\pm 35.5^\circ$  [Longuet-Higgins, 1976] as the narrowbanded assumption is to some extent respected (see Figure 1). However, for broader spectra, the energy tends to accumulate along directions wider than  $\pm 35.5^\circ$ . The angles formed with the mean wave direction, in particular, seem to weakly depend upon the initial degree of directional spreading: for a wavefield with an initial directional distribution corresponding to  $s_p = 48$ , the energy spreads on directions of about  $\pm 45^\circ$ ; for  $s_p = 24$ , the outward spreading of the energy occurs along directions of about  $\pm 50^\circ$ . The latter is consistent with previous simulations of the Euler equations performed by Tanaka [2001a], who also observed an accumulation of energy at directions of approximately  $\pm 50^\circ$ .

[24] We mention that the directional features of the nonlinear energy transfer are not macroscopically modified by the spectral peakedness (see, for example, Figures 4a and 4b). Nevertheless, there is a weak tendency to decrease the

angle of energy redistribution with decreasing initial peak enhancement factor. In this respect, for an initial sea states with  $\gamma = 1.0$  and  $s_p = 48$ , we observed that the energy tends to be redistributed toward a direction of about  $\pm 40^\circ$ .

#### 4. Evolution of the Directional Wave Spectrum

[25] In this section, we mainly discuss the effect of the energy transfer on the temporal evolution of the directional spectrum. Because similar qualitative results are obtained for all cases, the analysis is mainly concentrated on the wavefield with initial directional spreading coefficient  $s_p = 48$  and peak enhancement factor  $\gamma = 6.0$ . In Figure 5, snapshots of the wave spectrum at different time steps are presented.

[26] As a fraction of energy is moved toward lower wave numbers, a macroscopic change in the spectral density is observed in the form of a downshift of the spectral peak [see

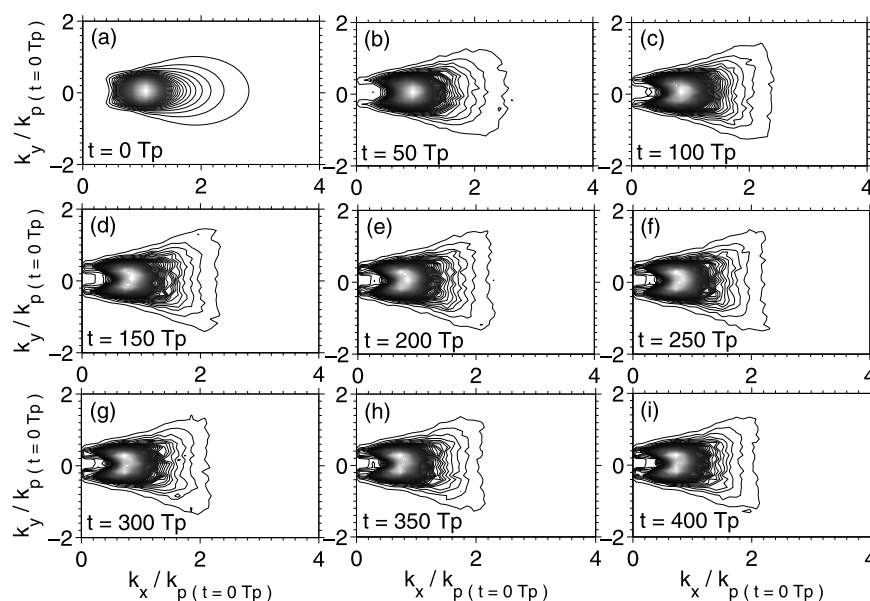


**Figure 5.** Temporal evolution of the directional spectrum with initial directional spreading  $s_p = 48$  and peak enhancement factor  $\gamma = 6.0$ .

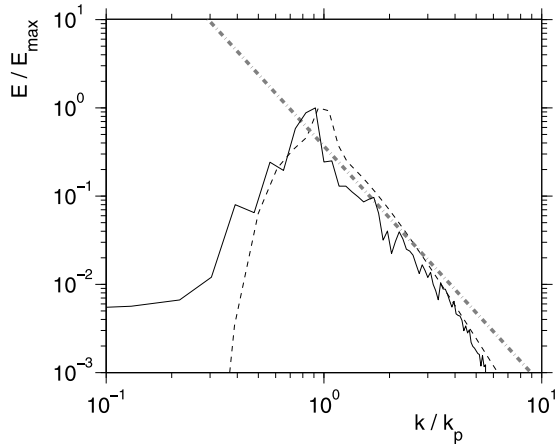


**Figure 6.** Evolution of the integrated wave number spectrum (initial  $s_p = 48$  and  $\gamma = 6.0$ ):  $t = 0 T_p$  (dashed line);  $t = 100 T_p$  (solid line); power law  $k^{-5/2}$  (dash-dotted line).

also Hasselmann, 1962; Onorato et al., 2002; Dysthe et al., 2003]. Furthermore, there is a relaxation of the spectral tail, which evolves toward a  $k^{-5/2}$  form [see Onorato et al., 2002; Dysthe et al., 2003]. These changes are shown in Figure 6, where the integrated wave number spectrum is presented. It is important to note, however, that because the energy is accumulated over two characteristic directions (see, e.g., Figure 2) the modality of the spectral peak is altered. This is highlighted in Figure 7, where the evolution of the spectral peak is presented. At the initial condition ( $t = 0 T_p$ ), the energy is concentrated on a narrow peak. As the wavefield evolves, the spectral bandwidth increases, especially along the  $k_y$  axis. After about 300 peak periods, which corresponds to a timescale of  $(\epsilon^3 \omega_p)^{-1}$ , the spectral peak develops bimodal properties, i.e., the energy is now concentrated over two separate spectral peaks. This finding is

consistent with recent long-term simulations of the Euler equations performed by Korotkevich et al. [2008], who also show the repartition of energy over two distinct directions at the spectral peak.

[27] A small fraction of energy is also transferred toward the short-wave portion of the spectrum (see Figure 2), resulting in a significant broadening of the directional spreading [cf. Banner and Young, 1994; Dysthe et al., 2003]. We observed that changes occur rather quickly within the first 150 peak periods, while the form of the directional distribution does not seem to vary substantially for longer time periods (see Figure 5). In order to quantify the spectral variation in the directional domain, the directional properties of the energy spectrum were summarized into a directional spread factor. The latter was calculated as the second-order moment of the directional distribution  $D$  expressed in  $(k, \vartheta)$  coordinates [see, e.g., Hwang et al., 2000]:

$$\sigma_2(k) = \left( \frac{\int_0^{\pi/2} \vartheta^2 D(k, \vartheta) d\vartheta}{\int_0^{\pi/2} D(k, \vartheta) d\vartheta} \right)^{1/2}. \quad (10)$$

[28] The directional spreading as a function of dimensionless wave numbers (for convenience, the peak wave number of the input spectrum is used as normalizing factor) is presented in Figure 8 for several time steps. For wave numbers nearby and above the spectral peak, the directional spreading enhances with respect to the initial condition; the variation is rather small around the energy peak, but it is significant in the short-wave portion of the spectrum. It is interesting to mention, however, that such changes are notable during the first 100–200 peak periods, and less evident for longer timescales. This is more clearly shown by the temporal evolution of the wave number average of

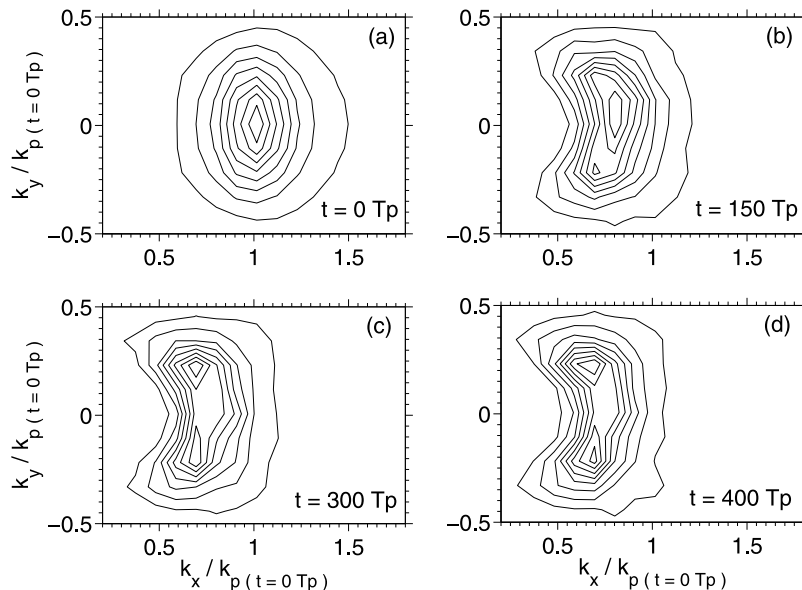


**Figure 7.** Temporal evolution of the spectral peak for a wavefield with initial directional spreading  $s_p = 48$  and  $\gamma = 6.0$ .

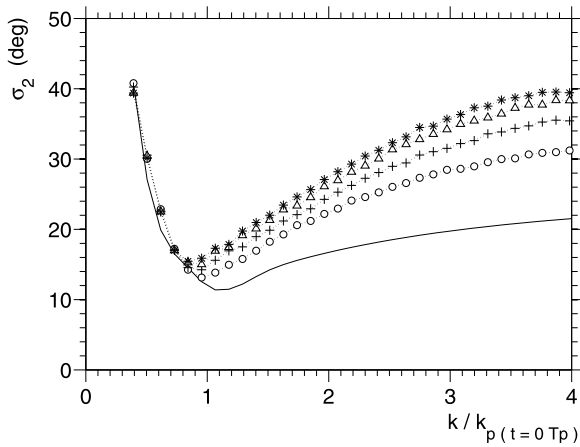


**Figure 8.** Temporal evolution of the directional spreading  $\sigma_2(k)$  for a wavefield with initial directional spreading  $s_p = 48$  and  $\gamma = 6.0$ :  $t = 0T_p$  (solid line);  $t = 100T_p$  (dots);  $t = 200T_p$  (pluses);  $t = 300T_p$  (triangles);  $t = 400T_p$  (asterisks).

the directional spread factor ( $\sigma_{2m}$ ), which is presented in Figure 9.

[29] If energy is moved toward two characteristic directions, the widening of the short-wave portion of the directional spectrum must be followed by an accumulation of energy in two sidelobes [see *Banner and Young, 1994*]. In Figure 10, for example, we show a cross section of the simulated spectrum at  $k_x = 3k_p$  for different time steps (for convenience, as in the work of *Hwang et al. [2000]*, the energy is normalized such that the magnitude at  $k_y = 0$  is unity). Similarly to what observed at the spectral peak (Figure 7), the wave energy migrates toward two symmetric sidelobes. It is interesting to note, however, that the development of the bimodal structure in the short wave part of the spectrum is more rapid than at the spectral peak; the existence of two separate lobes becomes already evident after about 150 peak periods.

[30] We now look at the temporal evolution of these sidelobes. This is presented in Figure 11, where the position of the maximal  $E(k_x, k_y)$  in the range  $-k_{y,max} \leq k_y \leq 0$ , and

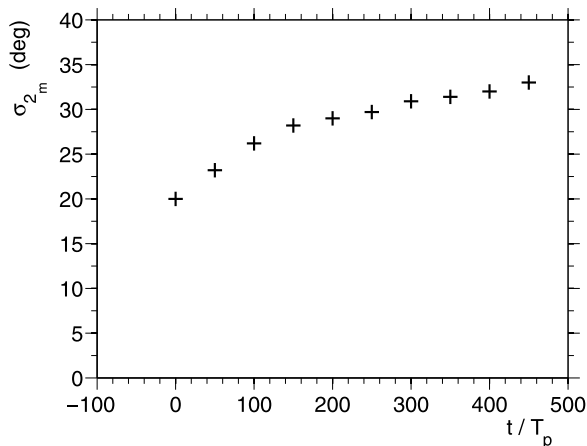


**Figure 9.** Temporal evolution of a frequency-average directional spreading for a wavefield with initial directional spreading  $s_p = 48$  and  $\gamma = 6.0$ .

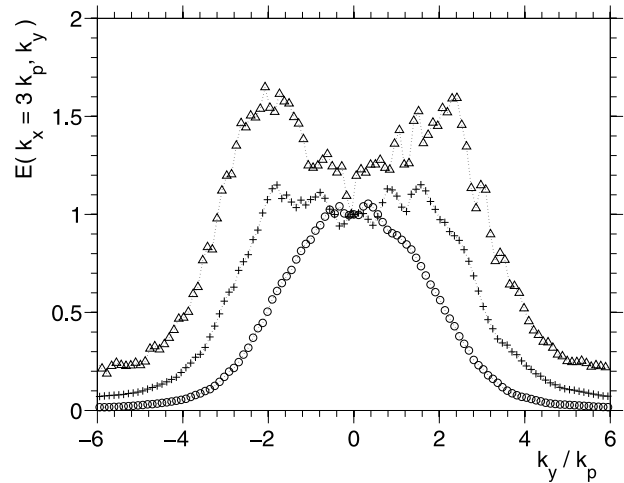


**Figure 10.** Cross section of the energy spectrum at  $k = 3k_p$  for a wavefield with initial directional spreading  $s_p = 48$  and  $\gamma = 6.0$ : After  $50T_p$  (dots); after  $150T_p$  (pluses); after  $300T_p$  (triangles).

likewise  $0 \leq k_y \leq k_{y,max}$ , is shown for several time steps; the peak wave number at each time step is here used as a normalizing factor, so that the peak period is always at  $k/k_p = 1$ ; the  $\pm 35.5^\circ$  directions for the energy transfer [*Longuet-Higgins, 1976*] are also presented as reference. During the first 50 peak periods, the spectrum retains its initial unimodal directional distribution (note, however, that the input spectrum allows directional bimodality at low wave numbers). As the wavefield evolves further, the energy is gradually shifted toward directions oblique to the dominant wave directions ( $k_x$  axis). After about 150 peak periods, two separate sidelobes have clearly developed in the short-wave portion of the energy spectrum. The lobes concentrate on directions close to  $\pm 35.5^\circ$  with respect to the  $k_x$  axis in agreement with *Longuet-Higgins [1976]*, mainly for  $k/k_p > 2$ . For a longer temporal evolution, however, the sidelobes tend to migrate toward broader directions. This deviation seems to take place for waves with wave number greater than  $3k_p$ , though. At time steps between 300 and 400 peak periods, nevertheless, the position of the lobes seems to stabilize as no significant changes are observed further (see Figures 11g, 11h, and 11i). For this timescale, the location of the sidelobes corresponds to the simulated patterns of the energy transfer (see Figure 2), even though a weak dependence upon the wave number can be observed.

[31] Although similar qualitative results are obtained for all selected directional wavefields, the angle at which the sidelobes concentrate weakly depends on the initial directional spreading as also observed for the energy transfer. In Figure 12 the position of the sidelobes for different initial directional wavefields is shown at a time step of 400 peak periods. For a fairly long crested wavefield ( $s_p = 180$ ), when the narrowbanded assumption is to a certain extent respected, the lobes distribute according to the  $\pm 35.5^\circ$  angles. For both short crested conditions, however, the sidelobes slightly migrate toward larger angles (see Figures 12b and 12c), mainly for  $k > 3k_p$ .

[32] The formation of the spectral lobes is also a distinctive feature in sea states with less-peaked spectral conditions (see Figure 13). However, we observed that there is a weak

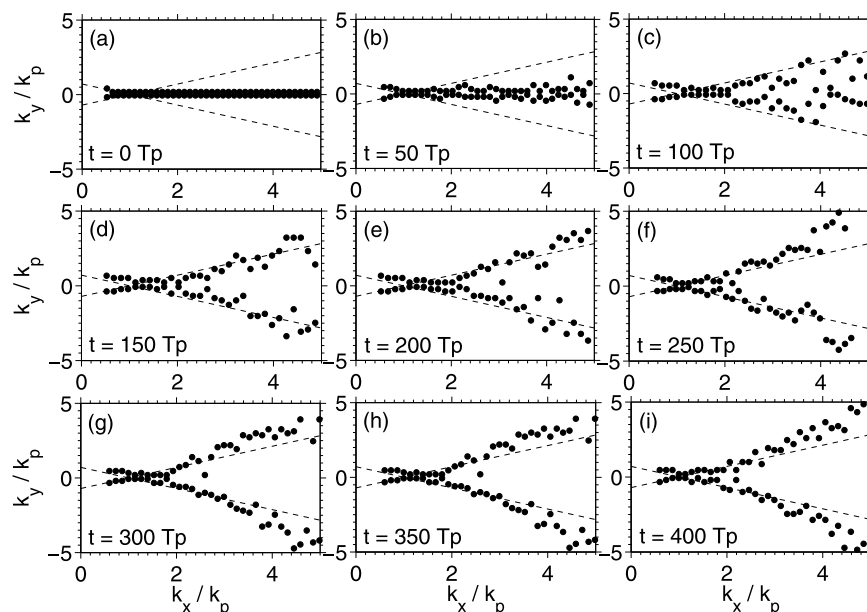


**Figure 11.** Temporal evolution of the lobe separation for a wavefield with initial directional spreading  $s_p = 48$  and  $\gamma = 6.0$  in  $(k_x, k_y)$  coordinates: Simulations (black dots);  $\pm 35.5^\circ$  directions [Longuet-Higgins, 1976] (dashed line).

tendency for the modal separation to decrease with decreasing spectral peakedness (in agreement with the energy redistribution). To some extent, this is consistent with field measurements by Long and Resio [2007], who observed a weak reduction of the angular separation between the lobes with increasing wave age.

## 5. Comparison With Field Observations

[33] The numerical simulations are here compared with field observations of bimodal directional distributions by Ewans [1998] and Hwang *et al.* [2000]. In order to quantify

the properties of the sidelobes, parameters related to their angular location and amplitude have been adopted in previous studies. Following Hwang *et al.* [2000], we used a representation of the wave spectrum from the  $(k, \vartheta)$  coordinates to compute such parameters. Thus, the angular location ( $\vartheta_{\text{Lobe}}$ ) is expressed as the direction associated with the maximal  $E(k, \vartheta)$  in the range  $-\pi/2 \leq \vartheta \leq 0$  (likewise for  $0 \leq \vartheta \leq \pi/2$ ). The lobe amplitude ( $r_{\text{Lobe}}$ ) is then expressed by the ratio of the maximal  $E(k, \vartheta)$  to its value at the dominant wave direction  $E(k, \vartheta_d = 0)$ .

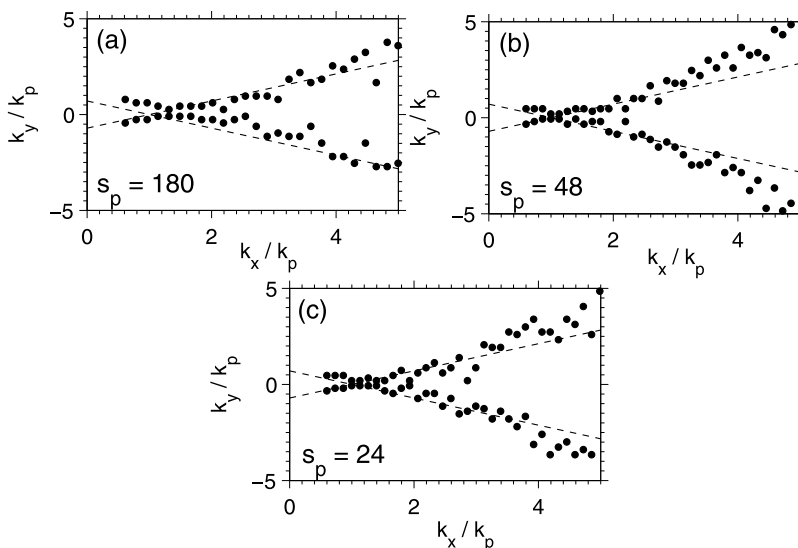


**Figure 12.** Lobe separation after  $400T_p$  for different directional wavefields in  $(k_x, k_y)$  coordinates: (a)  $s_p = 180$ ; (b)  $s_p = 48$ ; and (c)  $s_p = 24$ . Initial peak enhancement factor  $\gamma = 6.0$ . Simulations (black dots);  $\pm 35.5^\circ$  directions [Longuet-Higgins, 1976] (dashed line).

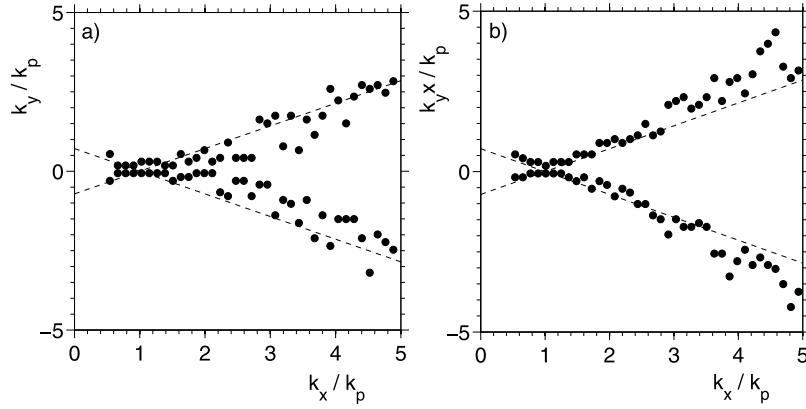


**Figure 13.** Lobe separation after  $400T_p$  for directional sea states with  $s_p = 48$  and peak enhancement factor (a)  $\gamma = 1$  and (b)  $\gamma = 3.0$ . The  $\pm 35.5^\circ$  directions [Longuet-Higgins, 1976] are presented as a dashed line.

### 5.1. Angular Position

[34] *Ewans* [1998] derived a parametric directional model, which was obtained by fitting a symmetric double Gaussian spectrum (bimodal wrapped Gaussian function) to measured spectra. Considering the symmetry between the two lobes, the angle (expressed in radians) between a sidelobe and the mean wave direction is as follows:

$$\vartheta_{\text{Lobe}} = \left(\frac{14.93}{2}\right) \frac{\pi}{180} \quad \text{for } f < f_p$$

$$\vartheta_{\text{Lobe}} = \left\{ \frac{1}{2} \exp \left[ 5.453 - 2.750 \left( \frac{f}{f_p} \right)^{-1} \right] \right\} \frac{\pi}{180} \quad \text{for } f \geq f_p,$$

(11)

where  $f$  is the wave frequency. According to linear theory, equation (11) can be adapted to  $(k, \vartheta)$  coordinates by substituting  $f/f_p$  with  $\sqrt{k/k_p}$ .

[35] *Hwang et al.* [2000] have used a polynomial fitting of their field measurements, in order to parameterize the angular position of the sidelobes. The resulting parametric curves are as follows:

$$\begin{aligned} \vartheta_{\text{Lobe}} &= -0.081 \left( \frac{k}{k_p} \right)^2 + 0.734 \left( \frac{k}{k_p} \right) - 0.739 & \text{for } \frac{k}{k_p} < 1.3 \\ \vartheta_{\text{Lobe}} &= 0.004 \left( \frac{k}{k_p} \right)^3 - 0.035 \left( \frac{k}{k_p} \right)^2 - 0.085 \left( \frac{k}{k_p} \right) + 0.235 & \text{for } \frac{k}{k_p} > 1.65. \end{aligned} \quad (12)$$

[36] The aforementioned parametric curves are here compared with numerical simulations. The temporal evolution of the angular location as a function of dimensionless wave numbers is presented in Figure 14 for a wavefield with initial directional spreading  $s_p = 48$  and  $\gamma = 6.0$ ; curves in equations (11) and (12) are also shown. For convenience,

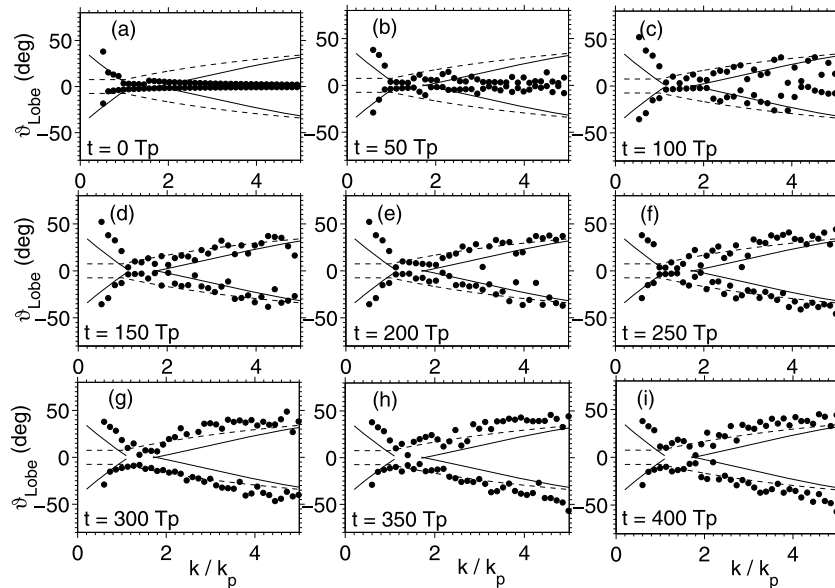


**Figure 14.** Temporal evolution of the lobe separation for a wavefield with initial directional spreading  $s_p = 48$   $\gamma = 6.0$ : parametric curves in *Ewans* [1998] (equation (11)) (dashed line); parametric curves in the work of *Hwang et al.* [2000] (equation (12)) (solid line); simulations (black dots).

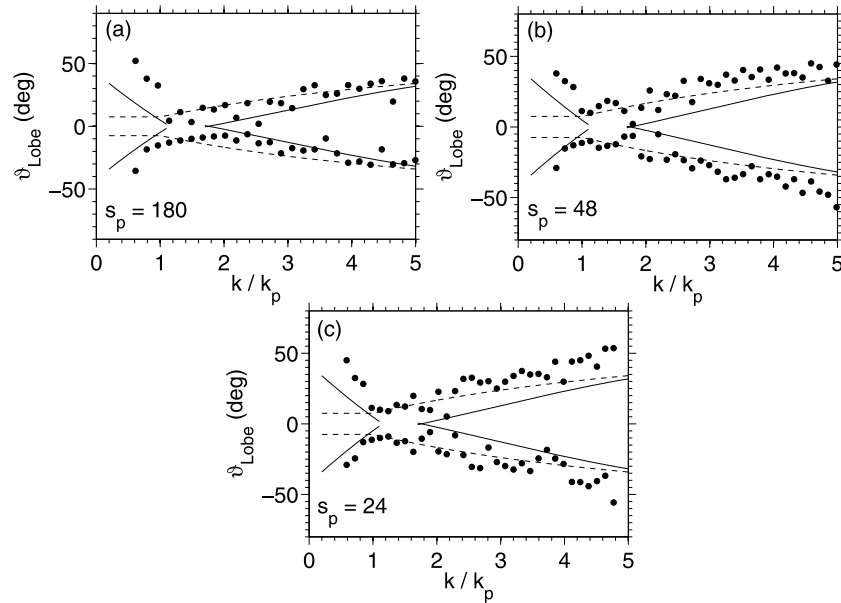


**Figure 15.** Lobe separation after  $400T_p$  for different directional wavefields: (a)  $s_p = 180$ ; (b)  $s_p = 48$ ; and (c)  $s_p = 24$ . Initial peak enhancement factor  $\gamma = 6.0$ . Parametric curves in *Ewans* [1998] (equation (11)) (dashed line); parametric curves in the work of *Hwang et al.* [2000] (equation (12)) (solid line); simulations (black dots).

wave numbers are normalized by the peak wave number at each time step.

[37] As previously observed (Figure 11), two distinct sidelobes occur after about 150 peak periods. A clear separation approximately begins at  $k > 1.6k_p$  in agreement with *Hwang et al.* [2000]. Furthermore, consistently with previous measurements [see, e.g., *Ewans*, 1998; *Hwang et al.*, 2000; *Wang and Hwang*, 2001], their angular position monotonically increases with the wave number. At this stage, the simulated angular position of the sidelobes slightly overpredicts the observations by *Hwang et al.* [2000] for  $k < 4k_p$ , while it better fits the measurements by *Ewans* [1998]. For very short waves ( $k > 4k_p$ ), the simulations agree well with both equations (11) and (12) that approximately coincide. In this respect, we mention that equation (12) is consistent with the numerical experiments by *Banner and Young* [1994] at very high wave numbers ( $k = 9k_p$ ), but it underpredicts the numerical results at  $k = 4k_p$  [see *Hwang et al.*, 2000, Figure 11].

[38] As the wavefield evolves further, the sidelobes migrated toward broader angles. After about 400 peak periods (when the angular location is approximately stable), the simulated results substantially deviate from equation (12), especially for  $k < 4k_p$ , while only slightly overestimate equation (11). Because the spectral peak also developed bimodal properties, the concentration of energy over two distinct directions is now visible on the entire range of wave numbers (i.e.,  $0 < k/k_p < 5$ ). The angle at which the energy concentrates is approximately  $\pm 10^\circ$  about the spectral peak, while it increases up to  $\pm 50^\circ$  for very short waves ( $k > 4k_p$ ). To some extent, these findings are consistent with numerical experiments by *Banner and Young* [1994] and *Gagnaire-Renou et al.* [2008] who investigated the formation of side lobes using the *Hasselmann* [1962] equation.

[39] In Figure 15, we compare the simulated angular separation after 400 peak periods for the three selected directional wavefields (i.e.,  $s_p = 180, 48, 24$ ). As discussed previously, the angular position of the lobes weakly depends upon the initial directional spreading. For a fairly long crested sea ( $s_p = 180$ ), we have observed that the directional bimodality is consistent with equation (11). As the initial directional spreading broadens,  $s_p = 48$  and 24, the sidelobes concentrate on slightly wider angles, deviating from equation (11) (see Figures 15b and 15c). However, for similar directional spreading, this deviation is slightly reduced by the spectral peakedness. Its effect is particularly evident for sea states with initial peak enhancement factor  $\gamma = 1.0$ , i.e., fully developed seas (see, for example, Figure 16).

## 5.2. Lobe Amplitude

[40] *Ewans* [1998] did not provide a parameterization for the lobe amplitude. However, an estimation can be derived directly from his parametric bimodal directional model:

$$D(f, \vartheta) = \frac{1}{\sqrt{8\pi}\sigma(f)} \sum_{n=-\infty}^{\infty} \left\{ \exp \left[ -\frac{1}{2} \left( \frac{\vartheta - \vartheta_1(f) - 2\pi n}{\sigma(f)} \right)^2 \right] + \exp \left[ -\frac{1}{2} \left( \frac{\vartheta - \vartheta_2(f) - 2\pi n}{\sigma(f)} \right)^2 \right] \right\}, \quad (13)$$

where  $\vartheta_1(f) = -\vartheta_2(f) = \vartheta_{\text{Lobe}}(f)$  (see equation (11)), and  $\sigma(f)$  is a spreading function defined as

$$\sigma(f) = 11.38 - 5.357 \left( \frac{f}{f_p} \right)^{-7.929} \quad \text{for } f < f_p$$

$$\sigma(f) = 32.13 - 15.39 \left( \frac{f}{f_p} \right)^{-2} \quad \text{for } f \geq f_p. \quad (14)$$

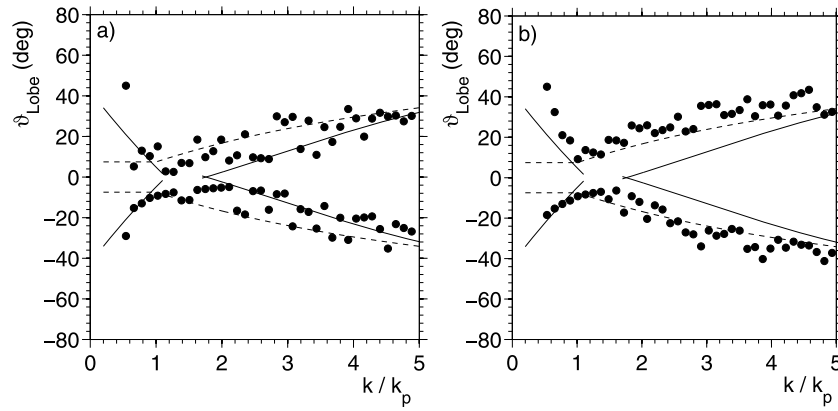


**Figure 16.** Lobe separation after  $400T_p$  for directional sea states with  $s_p = 48$  and peak enhancement factor (a)  $\gamma = 1$  and (b)  $\gamma = 3.0$ . Parametric curves in the work of *Ewans* [1998] (equation (11)) (dashed line); parametric curves in the work of *Hwang et al.* [2000] (equation (12)) (solid line); simulations (black dots).

Linear dispersion relation can then be used to move from  $(f, \vartheta)$  to  $(k, \vartheta)$  coordinates.

[41] On the basis of field measurements, *Hwang et al.* [2000] have provided parameterization curves describing the lobe amplitude as a function of  $k/k_p$ :

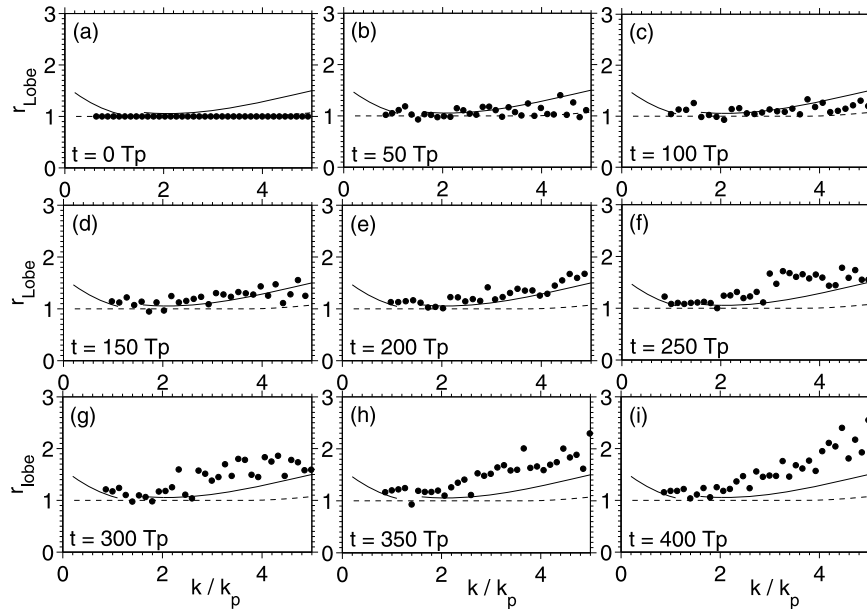
$$r_{\text{Lobe}} = 0.245 \left(\frac{k}{k_p}\right)^2 - 0.780 \left(\frac{k}{k_p}\right) + 1.610 \quad \text{for } \frac{k}{k_p} < 1.3$$

$$r_{\text{Lobe}} = -0.010 \left(\frac{k}{k_p}\right)^3 + 0.147 \left(\frac{k}{k_p}\right)^2 - 0.479 \left(\frac{k}{k_p}\right) + 1.509 \quad \text{for } \frac{k}{k_p} > 1.65. \quad (15)$$

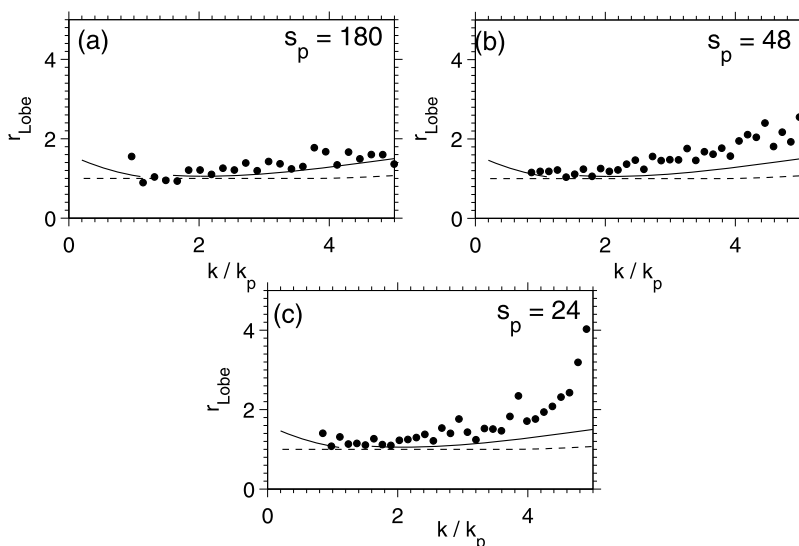
The evolution of the lobe amplitude for a simulated wavefield with initial  $s_p = 48$  and  $\gamma = 6.0$  is presented in

Figure 17; empirical results [i.e., *Ewans*, 1998; *Hwang et al.*, 2000] are reported for comparison.

[42] In the case of unimodal directional distribution, the lobe amplitude assumes values close to unity by definition. This is observed during the first 50 peak periods, when directional bimodality does not occur (see also Figure 14). As the wavefield evolves further, directional bimodality becomes evident and hence the lobe amplitude gradually deviates from unity. As also observed in situ [see, e.g., *Hwang et al.*, 2000; *Wang and Hwang*, 2001], the lobe amplitude increases toward the upper tail of the energy spectrum. For a time step of about 150 peak periods, when two distinct sidelobes are clearly visible in the short-wave part of the spectrum, the simulated lobe amplitude fits the parametric curves in equation (15), while it overestimates



**Figure 17.** Temporal evolution of the lobe amplitude for a wavefield with initial directional spreading  $s_p = 48$   $\gamma = 6.0$ : Parametric curves in the work of *Ewans* [1998] (derived from equation (13)) (dashed line); parametric curves in the work of *Hwang et al.* [2000] (equation (15)) (solid line); simulations (black dots).



**Figure 18.** Lobe amplitude after  $400T_p$  for different directional wavefields: (a)  $s_p = 180$ ; (b)  $s_p = 48$ ; and (c)  $s_p = 24$ . Initial peak enhancement factor  $\gamma = 6.0$ . Parametric curves in the work of *Ewans* [1998] (derived from equation (13)) (dashed line); parametric curves in the work of *Hwang et al.* [2000] (equation (15)) (solid line); simulations (black dots).

the lobe amplitude of the parametric bimodal directional model by *Ewans* [1998], where the lobes are less accentuated. On longer timescales, nevertheless, the simulated lobe amplitude further increases, deviating from the curves in equation (15); this result is consistent with measurements presented by *Wang and Hwang* [2001], where significant deviations from the observation by *Ewans* [1998] and *Hwang et al.* [2000] are shown. For time steps over 400 peak periods, changes in the lobe amplitude become negligible.

[43] In Figure 18, the lobe amplitude for three different directional wavefields is shown at a time step of 400 peak periods. It is interesting to see that the lobe amplitude is affected by the initial degree of directional spreading. For a long crested field ( $s_p = 180$ ), in fact, the sidelobes are less pronounced and the lobe amplitude fits the parametric curves in equation (15). However, as the initial directional

spreading increases, the lobe amplitude becomes gradually more accentuated (Figures 18b and 18c). Note that a similar, but less intense, dependence was also reported for the angular location. We mention, nonetheless, that the lobe's amplitude tends to be attenuated with the decreasing of the spectral peakedness (see Figure 19).

## 6. Conclusions

[44] Numerical simulations of the potential Euler equations were used to investigate the temporal evolution of directional wave spectra and, in particular, the development of sidelobes. In order to accomplish this task, a higher-order spectral method was used to integrate numerically the equations. A series of numerical experiments have been performed, considering both fairly long and short crested wavefields. For each of the selected sea states, an ensemble

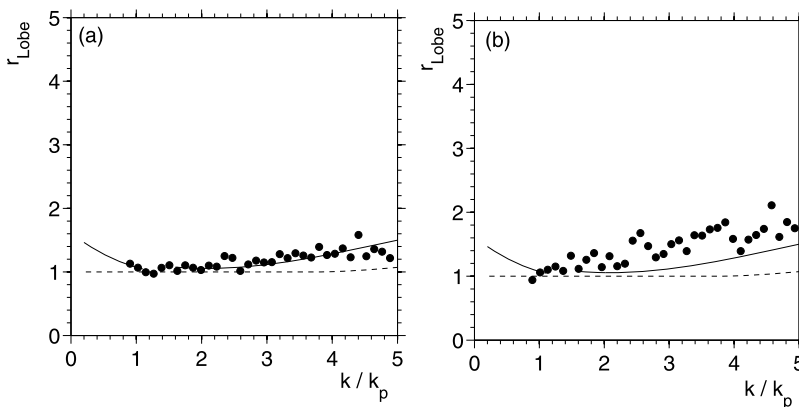


**Figure 19.** Lobe amplitude after  $400T_p$  for directional sea states with  $s_p = 48$  and peak enhancement factor (a)  $\gamma = 1$  and (b)  $\gamma = 3.0$ . Parametric curves in the work of *Ewans* [1998] (derived from equation (13)) (dashed line); parametric curves in the work of *Hwang et al.* [2000] (equation (15)) (solid line); simulations (black dots).

of 120 repetitions with different random amplitudes and phases has been made, in order to achieve statistically significant results. Note that because external forcing was not taken into account, only the effect of the nonlinear interaction was investigated.

[45] Simulations show that the nonlinear interactions spread energy outward the spectral peak along two characteristic directions in qualitative agreement with a simplified narrowbanded model proposed by *Longuet-Higgins* [1976]. According to the latter, in particular, the energy redistributes on directions forming angles of  $\pm 35.5^\circ$  with the dominant wave direction. Our numerical simulations, however, verified that this particular angular spreading only occurs when waves are fairly long crested such that the narrowbanded hypothesis is to some extent respected. For short crested waves, the outward spreading is shifted toward slightly broader directions. In this respect, there seems to exist a weak dependence upon the initial directional distribution: for  $s_p = 48$ , the energy redistributes on angles of  $\pm 45^\circ$ ; for  $s_p = 24$ , the energy redistributes on angles of  $\pm 50^\circ$ . Furthermore, we noted that the angle of the energy redistribution is also affected by the initial spectral peakedness. In this respect, we observed a weak reduction of this angle for decreasing spectral peakedness.

[46] As a result of the energy transfer, a gradual widening of the directional distribution is observed. For sufficiently long timescale, moreover, the spectral energy tends to concentrate on two symmetric sidelobes with directions oblique to the dominant wave direction, leading to a bimodal directional distribution. At an early stage of this process, directional bimodality only develops in the short-wave portion of the spectrum. As the wavefield evolves further, however, directional bimodality extends toward the spectral peak. The latter clearly assumes a bimodal form (i.e., the energy is concentrated on two distinct directions) for a timescale of about 300–400 peak periods. On this timescale, the directional distribution of the sidelobes corresponds to the patterns of the energy transfer. For longer timescales, no significant changes in the bimodal properties of the directional spectrum are observed.

[47] A comparison of the bimodal properties with field observations shows that the simulated angular position of the sidelobes is in agreement with a parametric bimodal directional model proposed by *Ewans* [1998], while it notably overpredicts the observations by *Hwang et al.* [2000], especially for  $k < 4k_p$ . It is interesting to note that the angular position of the lobes slightly depends upon the initial directional spreading. For a fairly long crested wavefield ( $s_p = 180$ ), the simulations fit the model by *Ewans* [1998]. However, as waves become more short crested, the sidelobes tend to slightly concentrate over broader directions with a consequent deviation from the aforementioned bimodal directional model.

[48] Despite the fact that the simulated angular position of the lobes is qualitatively represented by the model by *Ewans* [1998], the latter substantially underestimates the simulated lobe amplitudes. For fairly long crested conditions, the simulations fit the observations of *Hwang et al.* [2000], while a significant increase of the lobe amplitude is observed for short crested wavefields; this result is to some extent consistent with measurements presented by *Wang and Hwang* [2001]. It is also important to note that,

similarly to the angular position, a dependence upon the initial directional spreading was observed for the lobe amplitude.

[49] **Acknowledgments.** Financial support of the Australian Research Council and Woodside Energy Ltd. through the grant LP0883888 is also acknowledged. This work was carried out in the framework of the E.U. project SEAMOCS (contract MRTN-CT-2005-019374). Part of the numerical simulations were performed by using the K.U. Leuven's High Performance Computing (HPC) facilities.

## References

- Alves, J. H. G. M., and M. L. Banner (2003), Performance of a saturation-based dissipation-rate source term in modeling the fetch-limited evolution of wind waves, *J. Phys. Oceanogr.*, *33*, 1274–1298.
- Banner, M. L., and I. R. Young (1994), Modeling spectra dissipation in the evolution of wind waves. Part I: Assessment of existing model performance, *J. Phys. Oceanogr.*, *24*, 1550–1571.
- Clamond, D., M. Francius, J. Grue, and C. Kharif (2006), Long time interaction of envelope solitons and freak wave formations, *Eur. J. Mech. B*, *25*, 536–553.
- Coté, L. J., J. O. Davis, W. Marks, R. J. McGough, E. Mehr, W. J. Pierson, J. F. Ropek, G. Stephenson, and R. C. Vetter (1960), The directional spectrum of a wind generated sea as determined from data obtained by the Stereo Wave Observation Project, *Meteor. Pap.*, *2*, (6), pp. 1600–1604, New York Univ., New York.
- Davey, A., and K. Stewartson (1974), On three-dimensional packets of surface waves, *Proc. R. Soc. London, Sect. A*, *338*, 101–110.
- Dommermuth, D. G., and D. K. Yue (1987), A high-order spectral method for the study of nonlinear gravity waves, *J. Fluid Mech.*, *184*, 267–288.
- Donelan, M. A., J. Hamilton, and W. H. Hui (1985), Directional spectra of wind-generated waves, *Philos. Trans. R. Soc. London, Sect. A*, *315*, 509–562.
- Dysthe, K. B., K. Trulsen, H. Krogstad, and H. Socquet-Juglard (2003), Evolution of a narrow-band spectrum of random surface gravity waves, *J. Fluid Mech.*, *478*, 1–10.
- Ewans, K. C. (1998), Observations of directional spectrum of fetch-limited waves, *J. Phys. Oceanogr.*, *28*, 495–512.
- Gagnaire-Renou, E., M. Benoit, and P. Forget (2008), Modeling waves in fetch-limited and slanting fetch conditions using a quasi-exact method for nonlinear four-wave interaction, paper presented at 31st International Conference on Coastal Engineering, Hamburg, Germany.
- Goda, Y. (2000), Random seas and design on marine structures, in *Advanced Series on Ocean Engineering*, vol. 15, 443 pp., World Sci., Singapore.
- Hasselmann, D. E., M. Dunkel, and J. A. Ewing (1980), Directional wave spectra observed during JONSWAP 1973, *J. Phys. Oceanogr.*, *10*, 1264–1280.
- Hasselmann, K. (1962), On the non-linear energy transfer in a gravity-wave spectrum. Part I: General theory, *J. Fluid Mech.*, *12*, 481–500.
- Holthuijsen, L. H. (1983), Observation of the directional distribution of ocean wave energy in fetch-limited conditions, *J. Phys. Oceanogr.*, *13*, 191–203.
- Hwang, P. A., W. D. W., E. J. Walsh, W. B. Krabill, and R. N. Swift (2000), Airborne measurements of the wavenumber spectra of ocean surface waves. Part II: Directional distribution, *J. Phys. Oceanogr.*, *30*, 2768–2787.
- Jackson, F. C., W. T. Walton, and C. Y. Peng (1985), A comparison of in situ and airborne radar observations of ocean wave directionality, *J. Geophys. Res.*, *90*, 1005–1018.
- Janssen, P. A. E. M. (2004), *The Interaction of Ocean Waves and Wind*, 379 pp., Cambridge Univ. Press, Cambridge, U. K.
- Komen, G., L. Cavaleri, M. Donelan, K. Hasselmann, H. Hasselmann, and P. Janssen (1994), *Dynamics and Modeling of Ocean Waves*, Cambridge Univ. Press, Cambridge, U. K.
- Komen, G. J., S. Hasselmann, and K. Hasselmann (1984), On the existence of a fully developed wind-sea spectrum, *J. Phys. Oceanogr.*, *14*, 1271–1285.
- Korotkevich, A. O., A. Pushkarev, D. Resio, and V. E. Zakharov (2008), Numerical verification of the weak turbulent model for swell evolution, *Eur. J. Mech. B*, *27*(4), 361–387.
- Long, C. E., and D. T. Resio (2007), Wind wave spectral observations in Currituck Sound, North Carolina, *J. Geophys. Res.*, *112*, C05001, doi:10.1029/2006JC003835.
- Longuet-Higgins, F. R. S. (1976), On the nonlinear transfer of energy in the peak of a gravity-wave spectrum: a simplified model, *Proc. R. Soc. London, Sect. A*, *347*, 311–328.

- Lygre, A., and H. E. Krogstad (1986), Maximum entropy estimation of the directional distribution in ocean wave spectra, *J. Phys. Oceanogr.*, *16*, 2052–2060.
- Masuda, A. (1980), Nonlinear energy transfer between wind waves, *J. Phys. Oceanogr.*, *10*, 2082–2093.
- Mitsuyasu, H., F. Tasai, T. Suhara, S. Mizuno, M. Ohkusu, T. Honda, and K. Rikiishi (1975), Observations of the directional spectrum of ocean waves using a cloverleaf buoy, *J. Phys. Oceanogr.*, *5*, 750–760.
- Morland, L. C. (1996), Oblique wind waves generated by the instability of wind blowing over water, *J. Fluid Mech.*, *316*, 163–172.
- Onorato, M., A. R. Osborne, M. Serio, D. Resio, A. Puskarev, V. E. Zakharov, and C. Brandini (2002), Freely decaying weak turbulence for sea surface gravity waves, *Phys. Rev. Lett.*, *89*, 144501.
- Onorato, M., A. Osborne, M. Serio, L. Cavaleri, C. Brandini, and C. Stansberg (2006), Extreme waves, modulational instability and second order theory: Wave flume experiments on irregular waves, *Eur. J. Mech. B*, *25*, 586–601.
- Phillips, O. M. (1958), On some properties of the spectrum of wind generated ocean waves, *J. Mar. Res.*, *16*, 231–240.
- Phillips, O. M. (1960), On the dynamics of unsteady gravity waves of finite amplitude. Part 1, *J. Fluid Mech.*, *11*, 143–155.
- Tanaka, M. (2001a), Verification of Hasselmann's energy transfer among surface gravity waves by direct numerical simulations of primitive equations, *J. Fluid Mech.*, *444*, 199–221.
- Tanaka, M. (2001b), A method of studying nonlinear random field of surface gravity waves by direct numerical simulations, *Fluid Dyn. Res.*, *28*, 41–60.
- Tanaka, M. (2007), On the role of resonant interactions in the short-term evolution of deep-water ocean spectra, *J. Phys. Oceanogr.*, *37*, 1022–1036.
- Toffoli, A., E. Bitner-Gregersen, M. Onorato, and A. V. Babanin (2008), Wave crest and trough distributions in a broad-banded directional wave field, *Ocean Eng.*, *35*, 1784–1792.
- Tsai, W.-T., and D. K. Yue (1996), Computation of nonlinear free-surface flows, *Annu. Rev. Fluid Mech.*, *28*, 249–278.
- Wang, D. W., and P. A. Hwang (2001), Evolution of the bimodal directional distribution of ocean waves, *J. Phys. Oceanogr.*, *31*, 1200–1221.
- West, B. J., K. A. Brueckner, R. S. Jand, D. M. Milder, and R. L. Milton (1987), A new method for surface hydrodynamics, *J. Geophys. Res.*, *92*(C11), 11,803–11,824.
- Wyatt, L. R. (1995), The effect of fetch on the directional spectrum of Celtic Sea storm waves, *J. Phys. Oceanogr.*, *25*, 1550–1559.
- Young, I. R., and G. P. Van Vledder (1993), A review of the central role of nonlinear interactions in wind-wave evolution, *Philos. Trans. R. Soc. London, Sect. A*, *342*, 505–524.
- Young, I. R., L. A. Verhagen, and M. L. Banner (1995), A note on the bimodal directional spreading of fetch-limited wind waves, *J. Geophys. Res.*, *100*, 773–778.
- Zakharov, V. (1968), Stability of period waves of finite amplitude on surface of a deep fluid, *J. Appl. Mech. Tech. Phys.*, *9*, 190–194.
- 
- E. M. Bitner-Gregersen, Det Norske Veritas A.S., N-1322 Høvik, Norway.
- J. Monbaliu, Department of Civil Engineering, Katholieke Universiteit Leuven, B-3001 Heverlee, Belgium.
- M. Onorato, Dipartimento Fisica Generale, Università di Torino, I-10125 Torino, Italy.
- A. Toffoli, Faculty of Engineering and Industrial Sciences, Swinburne University of Technology, PO Box 218, Hawthorn, Vic 3122, Australia. (toffoli.alessandro@gmail.com)